We are IntechOpen, the world's leading publisher of Open Access books Built by scientists, for scientists

6,900
Open access books available

186,000
International authors and editors

200M
Downloads

Our authors are among the

154
Countries delivered to

TOP 1%
most cited scientists

12.2%
Contributors from top 500 universities

WEB OF SCIENCE™

Selection of our books indexed in the Book Citation Index in Web of Science™ Core Collection (BKCI)

Interested in publishing with us?
Contact book.department@intechopen.com

Numbers displayed above are based on latest data collected.
For more information visit www.intechopen.com

20

The Photonic Torque Microscope: Measuring Non-conservative Force-fields

Giovanni Volpe[1,2,3], Giorgio Volpe[1] and Giuseppe Pesce[4]
[1]*ICFO – The Institute of Photonic Sciences, Castelldefels (Barcelona),*
[2]*Max-Planck-Institut für Metallforschung, Stuttgart,*
[3]*Universität Stuttgart, Stuttgart,*
[4]*Università di Napoli "Federico II", Napoli,*
[1]*Spain*
[2,3]*Germany*
[4]*Italy*

1. Introduction

Over the last 20 years the advances of laser technology have permitted the development of an entire new field in optics: the field of *optical trapping and manipulation*. The focal spot of a highly focused laser beam can be used to confine and manipulate microscopic particles ranging from few tens of nanometres to few microns (Ashkin, 2000; Neuman & Block, 2004).

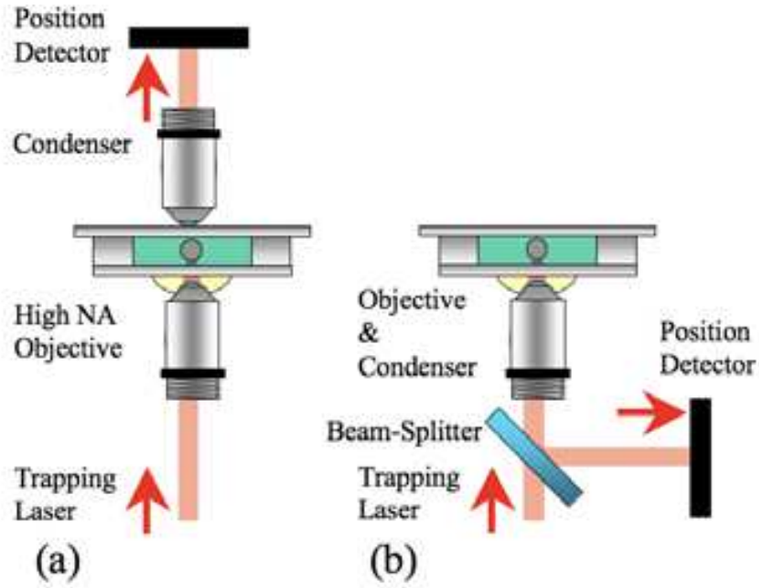

Fig. 1. PFM setups with detection using forward (a) and backward (b) scattered light.

Such an optical trap can detect and measure forces and torques in microscopic systems – a technique now known as photonic force microscope (PFM). This is a fundamental task in many areas, such as biophysics, colloidal physics and hydrodynamics of small systems.

Source: Recent Optical and Photonic Technologies, Book edited by: Ki Young Kim,
ISBN 978-953-7619-71-8, pp. 450, January 2010, INTECH, Croatia, downloaded from SCIYO.COM

The PFM was devised in 1993 (Ghislain & Webb, 1993). A typical PFM comprises an optical trap that holds a probe – a dielectric or metallic particle of micrometre size, which randomly moves due to Brownian motion in the potential well formed by the optical trap – and a position sensing system. The analysis of the thermal motion provides information about the local forces acting on the particle (Berg-Sørensen & Flyvbjerg, 2004). The PFM can measure forces in the range of femtonewtons to piconewtons. This range is well below the limits of techniques based on micro-fabricated mechanical cantilevers, such as the atomic force microscope (AFM).

However, an intrinsic limit of the PFM is that it can only deal with conservative force-fields, while it cannot measure the presence of a torque, which is typically associated with the presence of a non-conservative (or rotational) force-field.

In this Chapter, after taking a glance at the history of optical manipulation, we will briefly review the PFM and its applications. Then, we will discuss how the PFM can be enhanced to deal with non-conservative force-fields, leading to the photonic torque microscope (PTM) (Volpe & Petrov, 2006; Volpe et al., 2007a). We will also present a concrete analysis workflow to reconstruct the force-field from the experimental time-series of the probe position. Finally, we will present three experiments in which the PTM technique has been successfully applied:

1. *Characterization of singular points in microfluidic flows.* We applied the PTM to microrheology to characterize fluid fluxes around singular points of the fluid flow (Volpe et al., 2008).
2. *Detection of the torque carried by an optical beam with orbital angular momentum.* We used the PTM to measure the torque transferred to an optically trapped particle by a Laguerre-Gaussian beam (Volpe & Petrov, 2006).
3. *Quantitative measurement of non-conservative forces generated by an optical trap.* We used the PTM to quantify the contribution of non-conservative optical forces to the optical trapping (Pesce et al., 2009).

2. Brief history of optical manipulation

Optical trapping and manipulation did not exist before the invention of the laser in 1960 (Townes, 1999). It was already known from astronomy and from early experiments in optics that light had linear and angular momentum and, therefore, that it could exert radiation pressure and torques on physical objects. Indeed, light's ability to exert forces has been recognized at least since 1619, when Kepler's *De Cometis* described the deflection of comet tails by sunrays.

In the late XIX century Maxwell's theory of electromagnetism predicted that the light momentum flux was proportional to its intensity and could be transferred to illuminated objects, resulting in a radiation pressure pushing objects along the propagation direction of light.

Early exciting experiments were performed in order to verify Maxwell's predictions. Nichols and Hull (Nichols & Hull, 1901) and Lebedev (Lebedev, 1901) succeeded in detecting radiation pressure on macroscopic objects and absorbing gases. A few decades later, in 1936, Beth reported the experimental observation of the torque on a macroscopic object resulting from interaction with light (Beth, 1936): he observed the deflection of a quartz wave plate suspended from a thin quartz fibre when circularly polarized light passed through it. These effects were so small, however, that they were not easily detected. Quoting J. H. Poynting's

presidential address to the British Physical Society in 1905, "a very short experience in attempting to measure these forces is sufficient to make one realize their extreme minuteness – a minuteness which appears to put them beyond consideration in terrestrial affairs." (Cited in Ref. (Ashkin, 2000))

Things changed with the invention of the laser in the 1960s (Townes, 1999). In 1970 Ashkin showed that it was possible to use the forces of radiation pressure to significantly affect the dynamics of transparent micrometre sized particles (Ashkin, 1970). He identified two basic light pressure forces: a *scattering force* in the direction of the incident beam and a *gradient force* in the direction of the intensity gradient of the beam. He showed experimentally that, using just these forces, a focused laser beam could accelerate, decelerate and even stably trap small micrometre sized particles.

Ashkin considered a beam of power P reflecting on a plane mirror: $P/h\nu$ photons per second strike the mirror, each carrying a momentum $h\nu/c$, where h is the Planck constant, ν is the light frequency and c the speed of light. If they are all reflected straight back, the total change in light momentum per second is $2\cdot(P/h\nu)\cdot(h\nu/c)=2P/c$, which, by conservation of momentum, implies that the mirror experiences an equal and opposite force in the direction of the light. This is the maximum force that one can extract from the light. Quoting Ashkin (Ashkin, 2000), "Suppose we have a laser and we focus our one watt to a small spot size of about a wavelength $\cong 1\mu m$, and let it hit a particle of diameter also of $1\mu m$. Treating the particle as a 100% reflecting mirror of density $\cong 1 gm/cm^3$, we get an acceleration of the small particle $= A = F/m = 10^{-3} dynes / 10^{-12} gm = 10^9 cm/sec^2$. Thus, $A \cong 10^6 g$, where $g \cong 10^3 cm/sec^2$, the acceleration of gravity. This is quite large and should give readily observable effects, so I tried a simple experiment. [...] It is surprising that this simple first experiment [...], intended only to show forward motion due to laser radiation pressure, ended up demonstrating not only this force but the existence of the transverse force component, particle guiding, particle separation, and stable 3D particle trapping."

In 1986, Ashkin and colleagues reported the first observation of what is now commonly referred to as an *optical trap* (Ashkin et al., 1986): a tightly focused beam of light capable of holding microscopic particles in three dimensions. One of Ashkin's co-authors, Steven Chu, would go on to use optical tweezing in his work on cooling and trapping atoms. This research earned Chu, together with Claude Cohen-Tannoudji and William Daniel Phillips, the 1997 Nobel Prize in Physics.

In the late 1980s, the new technology was applied to the biological sciences, starting by trapping tobacco mosaic viruses and *Escherichia coli* bacteria. In the early 1990s, Block, Bustamante and Spudich pioneered the use of optical trap *force spectroscopy*, an alternate name for PFM, to characterize the mechanical properties of biomolecules and biological motors (Block et al., 1990; Finer et al., 1994; Bustamante et al., 1994). Optical traps allowed these biophysicists to observe the forces and dynamics of nanoscale motors at the single-molecule level. Optical trap force spectroscopy has led to a deeper understanding of the nature of these force-generating molecules, which are ubiquitous in nature.

Optical tweezers have also proven useful in many other areas of physics, such as atom trapping (Metcalf & van der Straten, 1999) and statistical physics (Babic et al., 2005).

3. The photonic force microscope

One of the most prominent uses of optical tweezers is to measure tiny forces, in the order of 100s of femtonewtons to 10s of piconewtons. A typical PFM setup comprises an optical trap

to hold a probe - a dielectric or metallic particle of micrometer size - and a position sensing system. In the case of biophysical applications the probe is usually a small dielectric bead tethered to the cell or molecule under study. The probe randomly moves due to Brownian motion in the potential well formed by the optical trap. Near the centre of the trap, the restoring force is linear in the displacement. The stiffness of such harmonic potential can be calibrated using the three-dimensional position fluctuations. To measure an external force acting on the probe it suffices to measure the probe average position displacement under the action of such force and multiply it by the stiffness.
In order to understand the PFM it is necessary to discuss these three aspects:

1. the *optical forces* that act on the probe and produce the optical trap;
2. the *position detection*, which permits one to track the probe position with nanometre resolution and at kilohertz sampling rate;
3. the statistics of the *Brownian motion* of the probe in the trap, which are used in the calibration procedure.

3.1 Optical forces

It is well known from quantum mechanics that light carries a momentum: for a photon at wavelength λ the associated momentum is $p = h/\lambda$. For this reason, whenever an atom emits or absorbs a photon, its momentum changes according to Newton's laws. Similarly, an object will experience a force whenever a propagating light beam is refracted or reflected by its surface. However, in most situations this force is much smaller than other forces acting on macroscopic objects so that there is no noticeable effect and, therefore, can be neglected. The objects, for which this radiation pressure exerted by light starts to be significant, weigh less than $1\mu g$ and their size is below 10s of microns.
A focused laser beam acts as an attractive potential well for a particle. The equilibrium position lies near – but not exactly at – the focus. When the object is displaced from this equilibrium position, it experiences an attractive force towards it. In first approximation this restoring force is proportional to the displacement; in other words, optical tweezers force can generally be described by Hooke's law:

$$F_x = -k_x (x - x_0), \tag{1}$$

where x is the particle's position, x_0 is the focus position and k_x is the spring constant of the optical trap along the x -direction, usually referred to as *trap stiffness*. In fact, an optical tweezers creates a three-dimensional potential well, which can be approximated by three independent harmonic oscillators, one for each of the x -, y- and z-directions. If the optics are well aligned, the x and y spring constants are roughly the same, while the z spring constant is typically smaller by a factor of 5 to 10.
Considering the ratio between the characteristic dimension L of the trapped object and the wavelength λ of the trapping light, three different trapping regimes can be defined:

1. the *Rayleigh regime*, when $L << \lambda$;
2. an *intermediate regime*, when L is comparable to λ;
3. the *geometrical optics regime*, when $L >> \lambda$.

In Fig. 2 an overview of the kind of objects belonging to each of these regimes is presented, considering that the trapping wavelength is usually in the visible or near-infrared spectral region. In any of these regimes, the electromagnetic equations can be solved to evaluate the

force acting on the object. However, this can be a cumbersome task. For the Rayleigh regime and geometrical optics regime approximate models have been developed. However, most of the objects that are normally trapped in optical manipulation experiments fall in the intermediate regime, where such approximations cannot be used. In particular, this is true for the probes usually used for the PFM: typically particles with diameter between 0.1 and 10 micrometres.

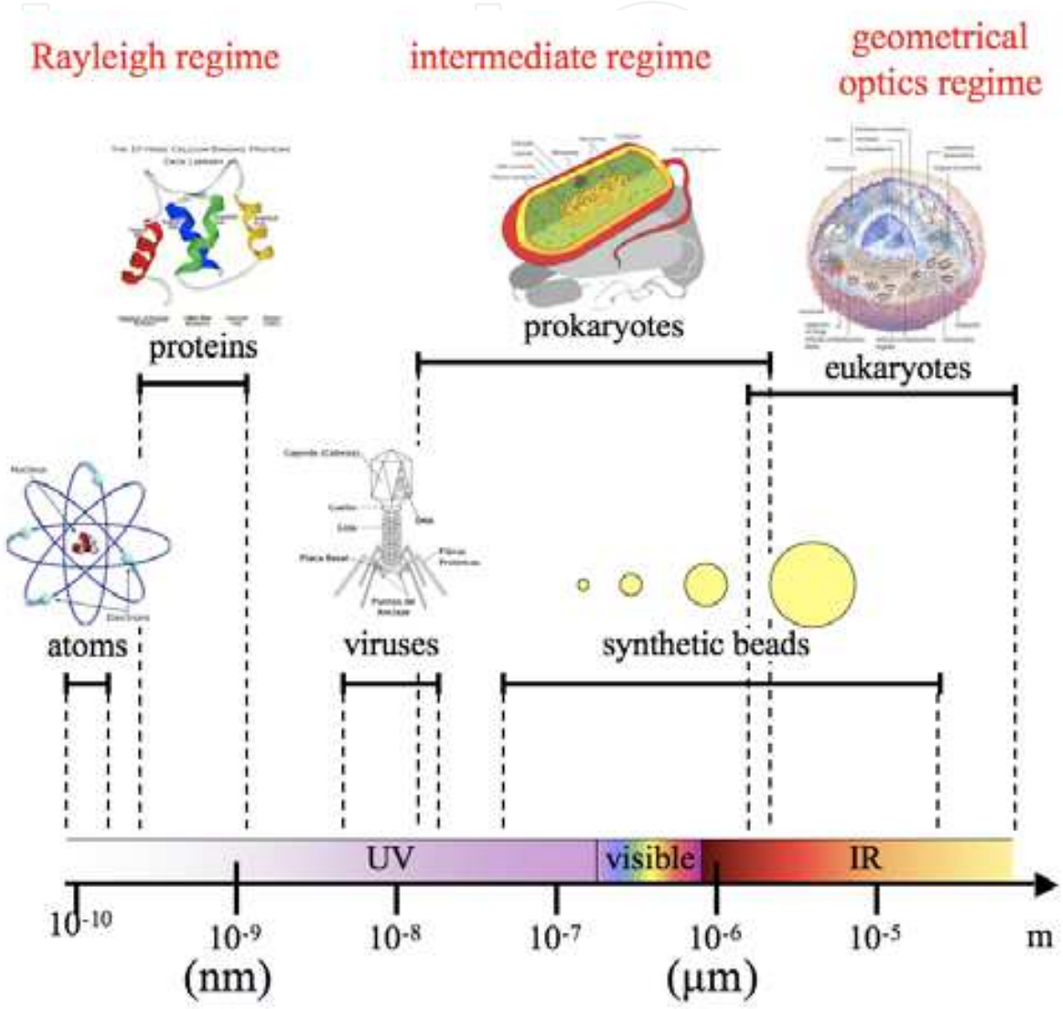

Fig. 2. Trapping regimes and objects that are typically optically manipulated: from cells to viruses in biophysical experiments, and from atoms to colloidal particles in experimental statistical physics. The wavelength of the trapping light is usually in the visible or near-infrared.

3.2 Position detection

The three-dimensional position of the probe is typically measured through the scattering of a light beam illuminating it. This can be the same beam used for trapping or an auxiliary beam.

Typically, position detection is achieved through the analysis of the interference of the forward-scattered (FS) light and unscattered (incident) light. A typical setup is shown in Fig.

1(a). The PFM with FS detection was extensively studied, for example, in Ref (Rohrbach & Stelzer, 2002).
In a number of experiments, however, geometrical constraints may prevent access to the FS light, forcing one to make use of the backward-scattered (BS) light instead. This occurs, for example, in biophysical applications where one of the two faces of a sample holder needs to be coated with some specific material or in plasmonics applications where a plasmon wave needs to be coupled to one of the faces of the holder (Volpe et al., 2006). A typical setup that uses the BS light is presented in Fig. 1(b). The PFM with BS detection has been studied theoretically in Ref. (Volpe et al., 2007b) and experimentally in Ref. (Huisstede et al., 2005).
Two types of photodetectors are typically used. The quadrant photodetector (QPD) works by measuring the intensity difference between the left-right and top-bottom sides of the detection plane. The position sensing detector (PSD) measures the position of the centroid of the collected intensity distribution, giving a more adequate response for non-Gaussian profiles. Note that high-speed video systems are also in use, but they do not achieve the acquisition rate available with photodetectors.

3.3 Brownian motion of an optically trapped particle

Assuming a very low Reynolds number regime (Happel & Brenner, 1983), the Brownian motion of the probe in the optical trap is described by a set of Langevin equations:

$$\gamma\,\mathbf{r}'(t) + \mathbf{K}\,\mathbf{r}(t) = \sqrt{2D}\,\gamma\,\mathbf{h}(t), \tag{2}$$

where $\mathbf{r}(t) = \left[x(t), y(t), z(t)\right]^T$ is the probe position, $\gamma = 6\pi R\eta$ its friction coefficient, R its radius, η the medium viscosity, $\mathbf{K}$ the stiffness matrix, $\sqrt{2D}\,\gamma\left[h_x(t), h_y(t), h_z(t)\right]^T$ a vector of independent white Gaussian random processes describing the Brownian forces, $D = k_B T / \gamma$ the diffusion coefficient, T the absolute temperature and k_B the Boltzmann constant. The orientation of the coordinate system can be chosen in such a way that the restoring forces are independent in the three directions, i.e. $\mathbf{K} = \mathrm{diag}\left(k_x, k_y, k_z\right)$. In such reference frame the stochastic differential Eqs. (2) are separated and, without loss of generality, the treatment can be restricted to the *x*-projection of the system.
When a constant and homogeneous external force $f_{ext,x}$ acting on the probe produces a shift in its equilibrium position in the trap, its value can be obtained as:

$$f_{ext,x} = k_x \left\langle x(t) \right\rangle, \tag{3}$$

where $\left\langle x(t) \right\rangle$ is the probe mean displacement from the equilibrium position.
There are several straightforward methods to experimentally measure the trap parameters – trap stiffness and conversion factor between voltage and length – and, therefore, the force exerted by the optical tweezers on an object, without the need for a theoretical reference model of the electromagnetic interaction between the particle and the laser beam. The most commonly employed ones are the *drag force method*, the *equipartition method*, the *potential analysis method* and the *power spectrum or correlation method* (Visscher et al., 1996; Berg-Sørensen & Flyvbjerg, 2004). The latter, in particular, is usually considered the most reliable one. Experimentally the trap stiffness can be found by fitting the autocorrelation function (ACF) of the Brownian motion in the trap obtained from the measurements to the theoretical one, which reads

$$r_{xx}(\tau) = \left\langle x(t+\tau)x^*(t) \right\rangle = \frac{k_B T}{k_x} e^{-\frac{k_x}{\gamma}|\tau|}. \quad (4)$$

4. The photonic torque microscope

The PFM measures a constant force acting on the probe. This implies that the force-field to be measured has to be invariable (homogeneous) on the scale of the Brownian motion of the trapped probe, i.e. in a range of 10s to 100s of nanometres depending on the trapping stiffness. In particular, as we will see, this condition implicates that the force-field must be conservative, excluding the possibility of a rotational component.

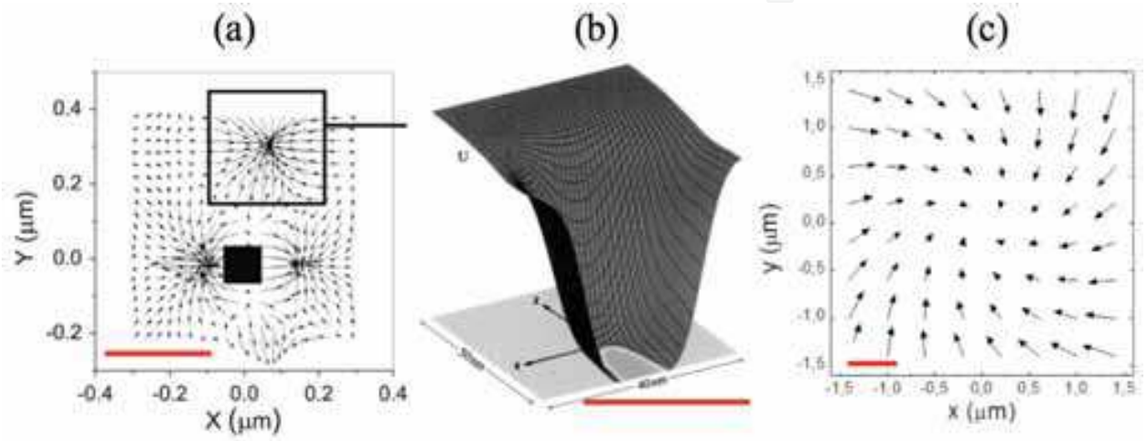

Fig. 3. Examples of physical systems that produce force-fields that cannot be correctly probed with a classical PFM, because they vary on the scale of the Brownian motion of the trapped probe (a possible range is indicated by the red bars): (a) forces produced by a surface plasmon polariton in the presence of a patterned surface on a 50*nm* radius dielectric particle (adapted from Ref. (Quidant et al., 2005)); (b) trapping potential for 10*nm* diameter dielectric particle near a 10*nm* wide gold tip in water illuminated by a 810*nm* monochromatic light beam (adapted from Ref. (Novotny et al., 1997)); and (c) force-field acting on a 500*nm* radius dielectric particle in the focal plane of a highly focused Laguerre-Gaussian beam (adapted from Ref. (Volpe & Petrov, 2006)).

However, there are cases where these assumptions are not fulfilled. The force-field can vary in the nanometre scale, for example, considering the radiation forces exerted on a dielectric particle by a patterned optical near-field landscape at an interface decorated with resonant gold nanostructures (Quidant et al., 2005) (Fig. 3 (a)), the nanoscale trapping that can be achieved near a laser-illuminated tip (Novotny et al., 1997) (Fig. 3(b)), the optical forces produced by a beam which carries orbital angular momentum (Volpe & Petrov, 2006) (Fig. 3(c)), or in the presence of fluid flows (Volpe et al., 2008). In order to deal with these cases, we need a deeper understanding of the Brownian motion of the optically trapped probe in the trapping potential.

In the following we will discuss the Brownian motion near an equilibrium point in a force-field and we will see how this permits us to develop a more powerful theory of the PFM: the Photonic Torque Microscope (PTM). Full details can be found in Ref. (Volpe et al., 2007a).

4.1 Brownian motion near an equilibrium position

In the presence of an external force-field $\mathbf{f}_{ext}(\mathbf{r}(t))$, Eq. (2) can be written in the form:

$$\gamma\,\mathbf{r}'(t) + \mathbf{f}(\mathbf{r}(t)) = \sqrt{2D}\,\gamma\,\mathbf{h}(t), \tag{5}$$

where the total force acting on the probe $\mathbf{f}(\mathbf{r}(t)) = \mathbf{f}_{ext}(\mathbf{r}(t)) - \mathbf{K}\mathbf{r}(t)$ depends on the position of the probe itself, but does not vary over time.

The force $\mathbf{f}(\mathbf{r}(t)) = \left[f_x(\mathbf{r}(t)), f_y(\mathbf{r}(t)) \right]^T$ can be expanded in Taylor series up to the first order around an arbitrary point $\mathbf{r}_0$:

$$\mathbf{f}(\mathbf{r}(t)) = \begin{bmatrix} f_x(\mathbf{r}_0) \\ f_y(\mathbf{r}_0) \end{bmatrix} + \begin{bmatrix} \dfrac{\partial f_x(\mathbf{r}_0)}{\partial x} & \dfrac{\partial f_x(\mathbf{r}_0)}{\partial y} \\ \dfrac{\partial f_y(\mathbf{r}_0)}{\partial x} & \dfrac{\partial f_y(\mathbf{r}_0)}{\partial y} \end{bmatrix} (\mathbf{r}(t) - \mathbf{r}_0) + o\left(\left\| \mathbf{r}(t) - \mathbf{r}_0 \right\| \right), \tag{6}$$

where $\mathbf{f}_{\mathbf{r}_0}$ and $\mathbf{J}_{\mathbf{r}_0}$ are the zeroth-order and first-order expansion coefficients, i.e. the force-field value at the point $\mathbf{r}_0$ and the Jacobian of the force-field calculated in $\mathbf{r}_0$. In the following we will assume, without loss of generality, $\mathbf{r}_0 = 0$.

In a PFM the probe is optically trapped and, therefore, it diffuses due to Brownian motion in the total force-field (the sum of the optical trapping force and external force-fields). If $\mathbf{f}_{\mathbf{r}_0} \neq 0$, the probe experiences a shift in the direction of the force and, after a transient time has elapsed, the particle settles down in a new equilibrium position of the total force-field, such that $\mathbf{f}_{\mathbf{r}_0} = 0$. As we have already seen, the measurement of this shift allows one to evaluate the homogeneous force acting on the probe in the standard PFM and, therefore, the zeroth order term of the Taylor expansion. In the following we will assume this to be null and study the statistics of the Brownian motion near the equilibrium point can be analyzed in order to reconstruct the force-field up to its first-order approximation.

4.2 Conservative and rotational components of the force-field

The first order approximation to Eq. (5) near an equilibrium point of the force-field, $\breve{\mathbf{r}} = 0$, is:

$$\mathbf{r}'(t) = \gamma^{-1}\,\mathbf{J}_0\,\mathbf{r}(t) + \sqrt{2D}\;\mathbf{h}(t), \tag{7}$$

where $\mathbf{r}(t) = \left[x(t), y(t) \right]^T$, $\mathbf{h}(t) = \left[h_x(t), h_y(t) \right]^T$ and $\mathbf{J}_0$ is the Jacobian calculated at the equilibrium point.

According to the Helmholtz theorem, any force-field can be separated into its conservative (irrotational) and non-conservative (rotational or solenoidal) components. With simple algebraic passages, the Jacobian $\mathbf{J}_0$ can be written as the sum of two matrices:

$$\mathbf{J}_0 = \mathbf{J}_{\mathbf{c}} + \mathbf{J}_{\mathbf{nc}}, \tag{8}$$

where

$$\mathbf{J}_{\mathbf{c}} = \begin{bmatrix} \dfrac{\partial f_x(\mathbf{0})}{\partial x} & \dfrac{1}{2}\left(\dfrac{\partial f_x(\mathbf{0})}{\partial y} + \dfrac{\partial f_y(\mathbf{0})}{\partial x} \right) \\ \dfrac{1}{2}\left(\dfrac{\partial f_y(\mathbf{0})}{\partial x} + \dfrac{\partial f_x(\mathbf{0})}{\partial y} \right) & \dfrac{\partial f_y(\mathbf{0})}{\partial y} \end{bmatrix} \tag{9}$$

and

$$\mathbf{J}_{\mathbf{nc}} = \begin{bmatrix} 0 & \frac{1}{2}\left(\frac{\partial f_x(\mathbf{0})}{\partial y} - \frac{\partial f_y(\mathbf{0})}{\partial x}\right) \\ \frac{1}{2}\left(\frac{\partial f_y(\mathbf{0})}{\partial x} - \frac{\partial f_x(\mathbf{0})}{\partial y}\right) & 0 \end{bmatrix}. \tag{10}$$

It is easy to show that $\mathbf{J}_c$ is the conservative component of the force-field and that $\mathbf{J}_{nc}$ is the rotational component.

The two components can be easily identified if the coordinate system is chosen such that $\frac{\partial f_x(\mathbf{0})}{\partial y} = -\frac{\partial f_y(\mathbf{0})}{\partial x}$. In this case, the Jacobian $\mathbf{J}_0$ normalized by the friction coefficient γ reads:

$$\gamma^{-1}\mathbf{J}_0 = \begin{bmatrix} -\phi_x & \Omega \\ -\Omega & -\phi_y \end{bmatrix}, \tag{11}$$

where $\phi_x = k_x / \gamma$, $\phi_y = k_y / \gamma$, $k_x = -\frac{\partial f_x(\mathbf{0})}{\partial x}$, $k_y = -\frac{\partial f_y(\mathbf{0})}{\partial y}$ and $\Omega = \gamma^{-1}\frac{\partial f_x(\mathbf{0})}{\partial y} = -\gamma^{-1}\frac{\partial f_y(\mathbf{0})}{\partial x}$.

In Eq. (11) the rotational component, which is invariant under a coordinate rotation, is represented by the non-diagonal terms of the matrix: Ω is the value of the constant angular velocity of the probe rotation around the *z*-axis due to the presence of the rotational force-field. The conservative component, instead, is represented by the diagonal terms of the Jacobian and is centrally symmetric with respect to the origin. Without loss of generality, it can be imposed that the stiffness of the trapping potential is higher along the *x*-axis, i.e. $k_x > k_y$ and, therefore, $\phi_x > \phi_y$.

4.3 Stability study

The conditions for the stability of the equilibrium point are

$$\begin{cases} \mathrm{Det}(\mathbf{J}_0) = \phi^2 - \Delta\phi^2 + \Omega^2 > 0 \\ \mathrm{Tr}(\mathbf{J}_0) = -2\phi < 0 \end{cases}, \tag{12}$$

where $\phi = (\phi_x + \phi_y)/2$ and $\Delta\phi = (\phi_x - \phi_y)/2$. The fundamental condition required to achieve the stability is $\phi > 0$. Assuming that this condition is satisfied, the behaviour of the optically trapped probe can be explored as a function of the parameters Ω/ϕ and $\Delta\phi/\phi$. The stability diagram is shown in Fig. 4(a).

The standard PFM corresponds to $\Delta\phi = 0$ and $\Omega = 0$. When a rotational term is added, i.e. $\Omega \neq 0$ and $\Delta\phi = 0$, the system remains stable. When there is no rotational contribution to the force-field ($\Omega = 0$) the equilibrium point becomes unstable as soon as $\Delta\phi \geq \phi$. This implicates that $\phi_y < 0$ and, therefore, the probe is not confined in the y-direction any more. In the presence of a rotational component ($\Omega \neq 0$) the stability region becomes larger; the equilibrium point now becomes unstable only for $\Delta\phi \geq \sqrt{\phi^2 - \Omega^2}$.

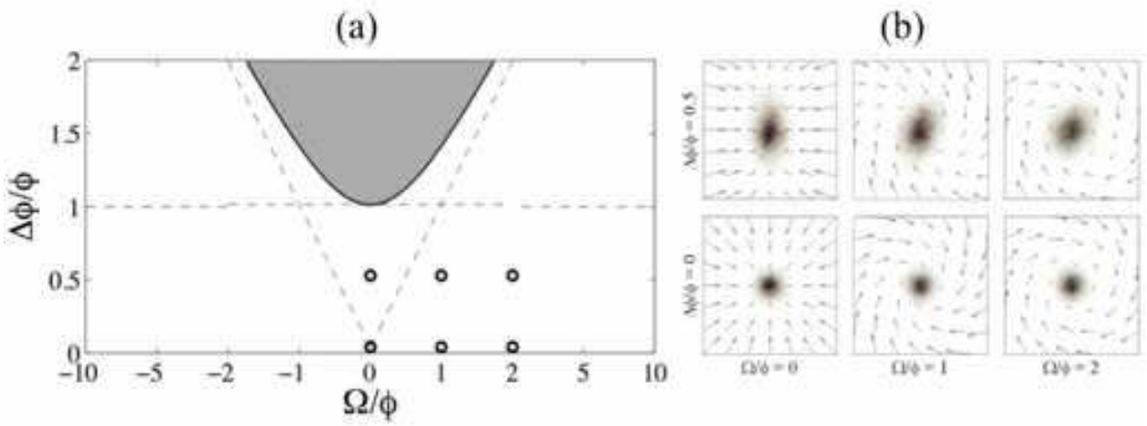

Fig. 4. (a) Stability diagram. Assuming φ > 0, the stability of the system is shown as a function of the parameters Ω/ϕ and $\Delta\phi/\phi$. The white region satisfies the stability conditions in Eq. (12). The dashed lines represent the $\Delta\phi = |\Omega|$ and $\Delta\phi = \phi$ curves. The dots represent the parameters that are further investigated in Figs. 4(b) and 5. (b) Brownian motion near an equilibrium point. The arrows show the force-field vectors for various values of the parameters Ω/ϕ and $\Delta\phi/\phi$. The shadowed areas show the probability distribution function (PDF) of the probe position in the corresponding force-field.

Some examples of possible force-fields are presented in Fig. 4(b). When $\Omega = 0$ the probe movement can be separated along two orthogonal directions. As the value of $\Delta\phi$ increases, the probability density function (PDF) of the probe position becomes more and more elliptical, until for $\Delta\phi \geq \phi$ the probe is confined only along the x-direction and the confinement along the y-direction is lost.
If $\Delta\phi = 0$, the increase in Ω induces a bending of the force-field lines and the probe movements along the x- and y-directions are not independent any more. For values of $\Omega \geq \phi$, the rotational component of the force-field becomes dominant over the conservative one. This is particularly clear when $\Delta\phi \neq 0$: the presence of a rotational component masks the asymmetry in the conservative one, since the PDF assumes a more rotationally symmetric shape.

4.4 The photonic torque microscope

The most powerful analysis method to characterize the stiffness of an optical trap is based on the study of the correlation functions - or, equivalently, of the power spectral density - of the probe position time-series. In order to derive the theory for the PTM, the correlation matrix for the general case of Eq. (5) will be first derived in the coordinate system considered in the previous section, where the conservative and rotational components are readily separated. Then, the same matrix will be given in a generic coordinate system and some invariant functions that are independent on its orientation will be identified.
Correlation matrix. The correlation matrix of the probe motion near an equilibrium position can be calculated from the solutions of Eq. (5). The full derivation is presented in Ref. (Volpe et al., 2007a). The correlation matrix results:

$$\begin{cases} r_{xx}(\Delta t) &= D\dfrac{e^{-\phi|\Delta t|}}{\phi}\left[\left(\dfrac{\Omega^2-\alpha^2\Delta\phi^2}{\Omega^2-\Delta\phi^2}-\alpha^2\dfrac{\Delta\phi}{\phi}\right)C(\Delta t)-\alpha^2\dfrac{\Delta\phi}{\phi}\left(1-\dfrac{\Delta\phi}{\phi}\right)S(|\Delta t|)\right] \\ r_{yy}(\Delta t) &= D\dfrac{e^{-\phi|\Delta t|}}{\phi}\left[\left(\dfrac{\Omega^2-\alpha^2\Delta\phi^2}{\Omega^2-\Delta\phi^2}+\alpha^2\dfrac{\Delta\phi}{\phi}\right)C(\Delta t)+\alpha^2\dfrac{\Delta\phi}{\phi}\left(1+\dfrac{\Delta\phi}{\phi}\right)S(|\Delta t|)\right] \\ r_{xy}(\Delta t) &= D\dfrac{e^{-\phi|\Delta t|}}{\phi}\dfrac{\Omega}{\phi}\left[+S(\Delta t)+\alpha^2\dfrac{\Delta\phi}{\phi}\left(C(\Delta t)+S(|\Delta t|)\right)\right] \\ r_{yx}(\Delta t) &= D\dfrac{e^{-\phi|\Delta t|}}{\phi}\dfrac{\Omega}{\phi}\left[-S(\Delta t)+\alpha^2\dfrac{\Delta\phi}{\phi}\left(C(\Delta t)+S(|\Delta t|)\right)\right] \end{cases}, \tag{13}$$

where

$$\alpha^2=\frac{\phi^2}{\phi^2+\left(\Omega^2-\Delta\phi^2\right)} \tag{14}$$

is a dimensionless parameter,

$$C(t)=\begin{cases}\cos\left(\sqrt{|\Omega^2-\Delta\phi^2|}t\right) & \Omega^2>\Delta\phi^2 \\ 1 & \Omega^2=\Delta\phi^2 \\ \cosh\left(\sqrt{|\Omega^2-\Delta\phi^2|}t\right) & \Omega^2<\Delta\phi^2\end{cases} \tag{15}$$

and

$$S(t)=\begin{cases}\phi\dfrac{\sin\left(\sqrt{|\Omega^2-\Delta\phi^2|}t\right)}{\sqrt{|\Omega^2-\Delta\phi^2|}} & \Omega^2>\Delta\phi^2 \\ \phi t & \Omega^2=\Delta\phi^2 \\ \phi\dfrac{\sinh\left(\sqrt{|\Omega^2-\Delta\phi^2|}t\right)}{\sqrt{|\Omega^2-\Delta\phi^2|}} & \Omega^2<\Delta\phi^2\end{cases}. \tag{16}$$

In Fig. 5(a) these correlation functions are plotted for different ratios of the force-field conservative and rotational components.

For the case $\Delta\phi=0$, the auto-correlation functions (ACFs) are $r_{xx}(\Delta t)=r_{yy}(\Delta t)=De^{-\phi|\Delta t|}\cos(\Omega\Delta t)/\phi$ and cross-correlation functions (CCFs) are $r_{xy}(\Delta t)=-r_{yx}(\Delta t)=De^{-\phi|\Delta t|}\sin(\Omega\Delta t)/\phi$. Their zeros are at $\Delta t=n\Omega/\pi$ and $\Delta t=(n+0.5)\Omega/\pi$ respectively, with n integer. However, when the rotational term is smaller than the conservative one ($\Omega<\phi$), the zeros are not distinguishable due to the rapid exponential decay of the correlation functions. As the rotational component becomes greater than the conservative one ($\Omega>\phi$), a first zero appears in the ACFs and CCFs and, as Ω increases even further, the number of oscillation grows. Eventually, for $\Omega>>\phi$ the sinusoidal component becomes dominant. The conservative component manifests itself as an exponential decay of the magnitude of the ACFs and CCFs.

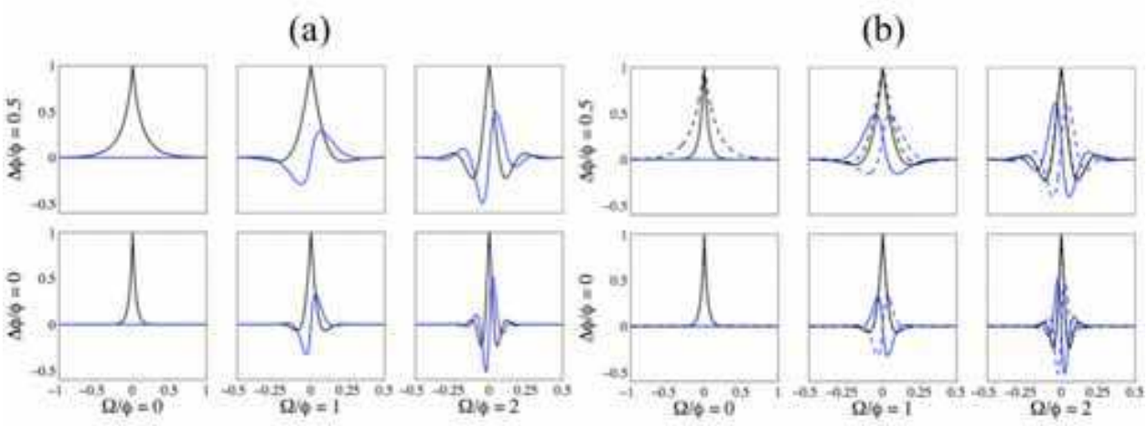

Fig. 5. (a) Autocorrelation and cross-correlation functions. Autocorrelation and cross-correlation functions for various values of the parameters Ω/ϕ and $\Delta\phi/\phi$: $r_{xx}(\Delta t)$ (black continuous line), $r_{yy}(\Delta t)$ (black dotted line), $r_{xy}(\Delta t)$ (blue continuous line) and $r_{yx}(\Delta t)$ (blue dotted line). (b) Invariant functions: $S_{ACF}(\Delta t)$ and $D_{CCF}(\Delta t)$. These functions, independent from the choice of the reference system, are presented for various values of the parameters Ω/ϕ and $\Delta\phi/\phi$: $S_{ACF}(\Delta t)$ (black line) and $D_{CCF}(\Delta t)$ (blue line).

When $\Omega = 0$, the movements of the probe along the x- and y-directions are independent. The ACFs are $r_{xx}(\Delta t) = De^{-\phi_x|\Delta t|}/\phi_x$ and $r_{yy}(\Delta t) = De^{-\phi_y|\Delta t|}/\phi_y$, while the CCFs are null, $r_{xy}(\Delta t) = r_{yx}(\Delta t) = 0$. In Fig. 4(a) this case is represented by the line $\Omega = 0$.

When both Ω and $\Delta\phi$ are zero, the ACFs are $r_{xx}(\Delta t) = r_{yy}(\Delta t) = De^{-\phi|\Delta t|}/\phi$ and the CCFs are null, i.e. $r_{xy}(\Delta t) = r_{yx}(\Delta t) = 0$. The corresponding force-field vectors point towards the centre and are rotationally symmetric.

When both Ω and $\Delta\phi$ are nonvanishing, the effective angular frequency that enters the correlation functions is given by $\sqrt{|\Omega^2 - \Delta\phi^2|}$. This shows that the difference in the stiffness coefficients along the *x*- and *y*-axes effectively influences the rotational term, if this is present. A limiting case is when $|\Omega| = \Delta\phi$. This case presents a pseudo-resonance between the rotational term and the stiffness difference.

Correlation matrix in a generic coordinate system. The expressions for the ACFs and CCFs in Eq. (13) were obtained in a specific coordinate system, where the conservative and rotational component of the force-field can be readily identified. However, the experimentally acquired time-series of the probe position required for the calculation of the ACFs and CCFs are usually given in a different coordinate system, rotated with respect to the one considered in the previous subsection. If a rotated coordinate system is introduced, such that

$$\mathbf{r}^{\theta}(t) = \mathbf{R}(\theta)\mathbf{r}(t), \tag{17}$$

where $\mathbf{r}^{\theta}(t) = \left[x^{\theta}(t), y^{\theta}(t)\right]^T$, $\mathbf{r}(t) = \left[x(t), y(t)\right]^T$ and $\mathbf{R}(\theta) = \begin{bmatrix} \cos\theta & -\sin\theta \\ \sin\theta & \cos\theta \end{bmatrix}$, the correlation functions in the new system are given by

$$\begin{bmatrix} r_{xx}^{\theta}(\Delta t) & r_{xy}^{\theta}(\Delta t) \\ r_{yx}^{\theta}(\Delta t) & r_{yy}^{\theta}(\Delta t) \end{bmatrix} = \begin{bmatrix} \cos\theta & -\sin\theta \\ \sin\theta & \cos\theta \end{bmatrix} \begin{bmatrix} r_{xx}(\Delta t) & r_{xy}(\Delta t) \\ r_{yx}(\Delta t) & r_{yy}(\Delta t) \end{bmatrix}, \tag{18}$$

which in general depend on the rotation angle θ.

However, it is remarkable that the difference of the two CCFs, $D_{CCF}(\Delta t) = r_{xy}^{\theta}(\Delta t) - r_{yx}^{\theta}(\Delta t)$, and the sum of the ACFs, $S_{ACF}(\Delta t) = r_{xx}^{\theta}(\Delta t) + r_{yy}^{\theta}(\Delta t)$, are invariant with respect to θ:

$$D_{CCF}(\Delta t) = 2D\frac{e^{-\phi|\Delta t|}}{\phi}\frac{\Omega}{\phi}S(\Delta t) \tag{19}$$

and

$$S_{ACF}(\Delta t) = 2D\frac{e^{-\phi|\Delta t|}}{\phi}\left[\left(\frac{\Omega^2 - \alpha^2\Delta\phi^2}{\Omega^2 - \Delta\phi^2} + \alpha^2\frac{\Delta\phi}{\phi}\right)C(\Delta t) + \alpha^2\frac{\Delta\phi^2}{\phi^2}S(|\Delta t|)\right]. \tag{20}$$

These functions are presented in Fig. 5(b).

Other two combinations of the correlation functions, which are also useful for the analysis of the experimental data, namely the sum of the CCFs, $S_{CCF}(\Delta t,\theta) = r_{xy}^{\theta}(\Delta t) + r_{yx}^{\theta}(\Delta t)$, and the difference of the ACFs, $D_{ACF}(\Delta t,\theta) = r_{xx}^{\theta}(\Delta t) - r_{yy}^{\theta}(\Delta t)$, depend on the choice of the reference frame:

$$S_{CCF}(\Delta t,\theta) = 2D\frac{e^{-\phi|\Delta t|}}{\phi}\alpha^2\frac{\Delta\phi^2}{\phi^2}\left(C(\Delta t) + S(|\Delta t|)\right)\left(\frac{\Omega}{\phi}\cos(2\theta) - \sin(2\theta)\right) \tag{21}$$

and

$$D_{ACF}(\Delta t,\theta) = -2D\frac{e^{-\phi|\Delta t|}}{\phi}\alpha^2\frac{\Delta\phi^2}{\phi^2}\left(C(\Delta t) + S(|\Delta t|)\right)\left(\frac{\Omega}{\phi}\sin(2\theta) + \cos(2\theta)\right). \tag{22}$$

In particular, they deliver information on the orientation θ of the coordinate system.

4.5 Torque detection using brownian fluctuations

We have seen that any force-field acting on a Brownian particle can be readily separated into its irrotational and rotational components. The last one, in particular, is completely defined by the value of the constant angular velocity Ω of the probe rotation around the z-axis. Such a rotation can be produced by the action of mechanical torque acting on the particle.

Once the value of Ω is known, the torque can be quantified. The constant angular velocity Ω results from a balance between the torque applied to the particle and the drag torque: $\tau_{\mathbf{drag}} = \mathbf{r}\times\mathbf{F}_{\mathbf{drag}} = \gamma\mathbf{r}\times\mathbf{v} = \gamma\mathbf{r}\times(\mathbf{r}\times\Omega)$, where $\mathbf{r}$ is the particle position and $\mathbf{v}$ is its linear velocity. Hence, the force acting on the particle from the torque source is given by $\mathbf{F} = \gamma\mathbf{r}\times\Omega$, which depends on the position of the particle. A time average of the torque exerted on the particle can then be expressed as

$$\langle\tau\rangle = \gamma\langle\mathbf{r}\times(\mathbf{r}\times\Omega)\rangle = \gamma\Omega\langle r^2\rangle \tag{23}$$

where $\langle r^2 \rangle$ is the mean square displacement of the sphere in the plane orthogonal to the torque.

With Eq. (23) we were able to measure torques in the range between 10s to 100s $fN\,\mu m$. The value of the measured torques (e.g. $4\,fN\,\mu m$ in Ref. (Volpe & Petrov, 2006)) is lower than the ones previously reported: $50\,fN\,\mu m$ for DNA twist elasticity (Bryant et al., 2003), $5 \cdot 10^3\,fN\,\mu m$ for the movement of bacterial flagellar motors (Berry & Berg, 1997), $20 \cdot 10^3\,fN\,\mu m$ for the transfer of orbital optical angular momentum (Volke-Sepulveda et al., 2002), or $5 \cdot 10^2\,fN\,\mu m$ for the transfer of spin optical angular momentum (La Porta & Wang, 2004).

5. Data analysis workflow

The experimental position time-series need to be statistically analyzed in order to reconstruct all the parameters of the force-field, i.e. ϕ, $\Delta\phi$ and Ω, and the orientation of the coordinate system θ.

Supposing to have the probe position time-series in the experimental coordinate system $\mathbf{r}^e(t) = \left[x^e(t), y^e(t)\right]^T$, the data analysis procedure consists of three steps:

1. Evaluation of the parameters ϕ, $\Delta\phi$ and Ω;
2. Orientation of the coordinate system;
3. Reconstruction of the total force-field and subtraction of the trapping force-field to retrieve the external force-field under investigation.

In order to illustrate this method we proceed to analyze some numerically simulated data. The main steps of this analysis are presented in Fig. 6. In Fig. 6(a) the PDF is shown for the case of a probe in a force-field with the following parameters: $\phi = 37 s^{-1}$, $\Delta\phi = 9.3 s^{-1}$ (corresponding to $k_x = 43 pN/\mu m$ and $k_y = 26 pN/\mu m$), $\Omega = 0$ and $\theta = 30^\circ$. The PDF is ellipsoidal due to the difference of the stiffness along two orthogonal directions. In Fig. 6(b) the PDF for a force-field with the same ϕ, $\Delta\phi$ and orientation, but with $\Omega = 37 s^{-1}$ is presented. The two time-series are chosen to have the same value of the parameters, except for Ω, in order to show not only how the method can obtain reliable estimates for the parameters, but also how it can distinguish between completely different physical situations, such as the absence or the presence of a non-conservative effect. The presence of the rotational component in the force-field produces two main effects. First, the PDF is more rotationally-symmetric and its main axes undergo a further rotation. Secondly, $D_{CCF}(\Delta t)$ is not null (Fig. 6(d)).

5.1 Estimation of the parameters

In order to evaluate the force-field parameters ϕ, $\Delta\phi$ and Ω the first step is to calculate the correlation matrix in the coordinate system where the experiment has been performed. $D_{CCF}(\Delta t)$ is invariant with respect to the choice of the reference system and it is different from zero only if $\Omega \neq 0$. The results are shown in Fig. 6(c) and Fig. 6(d) for the cases of the data shown in Fig. 6(a) and Fig. 6(b) respectively. The three aforementioned parameters can be found by fitting the experimental $D_{CCF}(\Delta t)$ to its theoretical shape.

When $\Omega = 0$, the $D_{CCF}(\Delta t)$ is null, as it can be seen also in Fig. 6(c), and, therefore, it cannot be used to find the two remaining parameters. For $\Omega = 0$, the other invariant function,

$S_{ACF}(\Delta t)$ can be used to evaluate ϕ and $\Delta\phi$. In general, $S_{ACF}(\Delta t)$ can also be used for the fitting of all the three parameters, but cannot give information on the sign of Ω, which must be retrieved from the sign of the slope at $\Delta t = 0$ of $D_{CCF}(\Delta t)$.

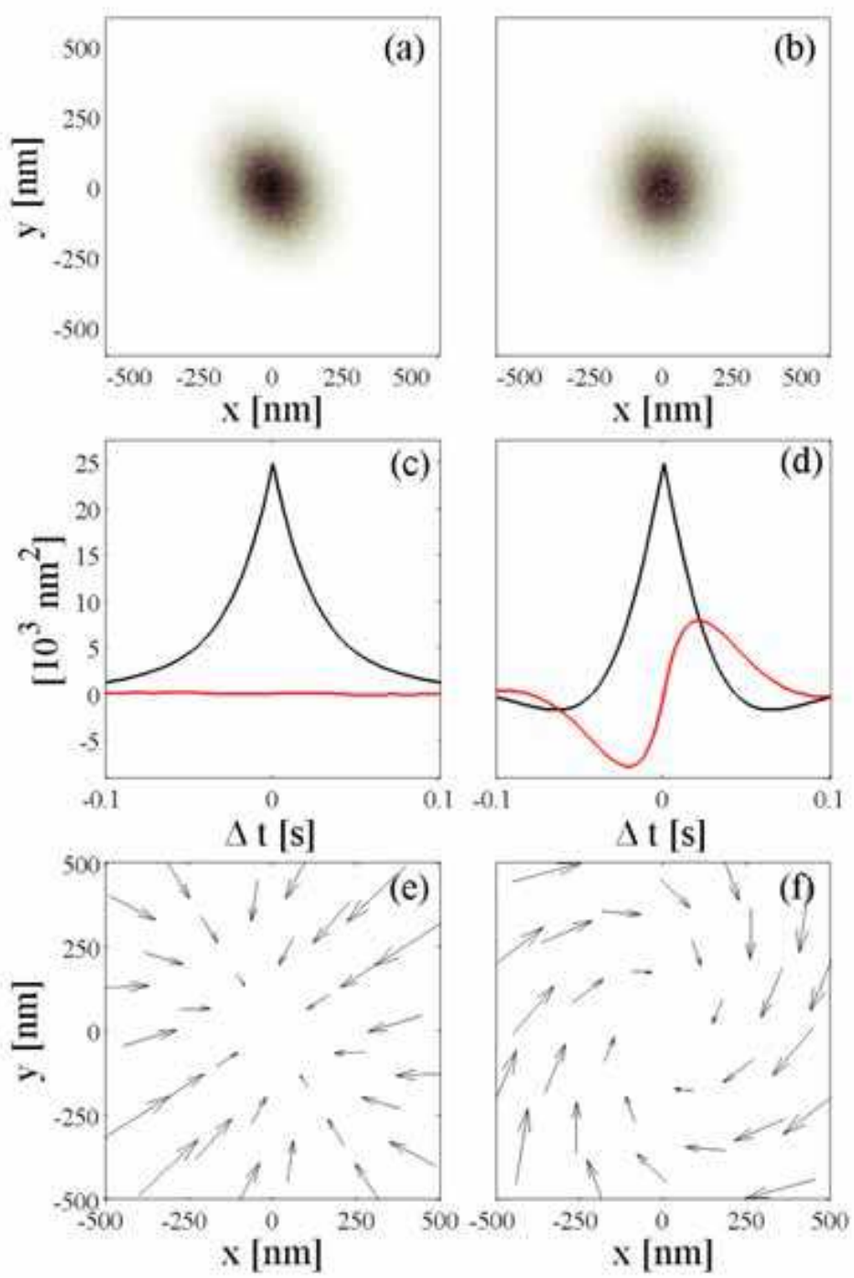

Fig. 6. Data analysis of numerically simulated time-series. (a-b) Probability density function for a Brownian particle under the influence of the force-field (simulated data $30s$ at $16kHz$); in (a) the force-field is purely conservative, while in (b) it has a rotational component. (c-d) Invariant function, $S_{CCF}(\Delta t)$ (black line) and $D_{CCF}(\Delta t)$ (red line) calculated from the simulated data and (e-f) reconstructed force-fields.

5.2 Orientation of the coordinate system

Although the values of the parameters ϕ, $\Delta\phi$ and Ω are now known, the directions of the force vectors are still missing. In order to retrieve the orientation of the experimental coordinate system, the orientation dependent functions $S_{CCF}(\Delta t,\theta)$ and $D_{ACF}(\Delta t,\theta)$ can be used. The best choice is to evaluate the two functions for $\Delta t = 0$, because the signal-to-noise ratio is highest at this point. The solution of this system delivers the value of the rotation angle θ:

$$\sin(2\theta) = \frac{\frac{\Omega}{\phi} D_{ACF}(0,\theta) - S_{CCF}(0,\theta)}{1 - 2D\frac{\alpha^2}{\phi}\frac{\Delta\phi}{\phi}\left(\frac{\Omega}{\phi}\right)^2}. \tag{24}$$

If $\Delta\phi = 0$, the value of θ is undetermined as a consequence of the PDF radial symmetry. In this case any orientation can be used. If $\Omega = 0$, the orientation of the coordinate system coincides with the axis of the PDF ellipsoid and, although Eq. (24) can still be used, the Principal Component Analysis (PCA) algorithm applied on the PDF is a convenient means to determine their directions.

5.3 Reconstruction of the force-field

Now everything is ready to reconstruct the unknown force-field acting on the probe around the equilibrium position. From the values of ϕ and $\Delta\phi$, the conservative forces acting on the probe result in $\mathbf{f_c}(x,y) = -\left(k_x x\mathbf{e}_x + k_y y\mathbf{e}_y\right)$ and, from the values of Ω, the rotational force is $\mathbf{f}_r(x,y) = \Omega\left(y\mathbf{e}_x - x\mathbf{e}_y\right)$. The total force-field is, therefore,

$$\mathbf{f}(x,y) = \mathbf{f_c}(x,y) + \mathbf{f}_r(x,y) = \left(-k_x x + \Omega y\right)\mathbf{e}_x + \left(-k_y y - \Omega x\right)\mathbf{e}_y \tag{25}$$

in the rotated coordinate system (Figs. 6(e) and 6(f)). Eq. (17) can be used to have the force-field in the experimental coordinate system. The unknown component can be easily reconstructed by subtraction of the known ones, such as the optical trapping force-field.

6. Applications: characterization of microscopic flows

The experimental characterization of fluid flows in micro-environments is important both from a fundamental point of view and from an applied one, since for many applications, such as lab-on-a-chip devices, it is required to assess the performance of microfluidic structures. Carrying out this kind of measurements can be extremely challenging. In particular, due to the small size of these environments, wall effects cannot be neglected. Additional difficulties arise studying biological fluids because of their complex rheological properties.

Following the data workflow presented in the previous section, the Brownian motion of an optically trapped polystyrene sphere in the presence of an external force-field generated by a fluid flow is analyzed (Volpe et al., 2008). Experimentally, two basic kinds of force-field –

namely a conservative force-field and a purely rotational one – are generated using solid spheres made of a birefringent material (Calcium Vaterite Crystals (CVC) spheres, radius $R = 1.5 \pm 0.2 \mu m$), which can be made spin through the transfer of light orbital angular momentum (Bishop et al., 2004).

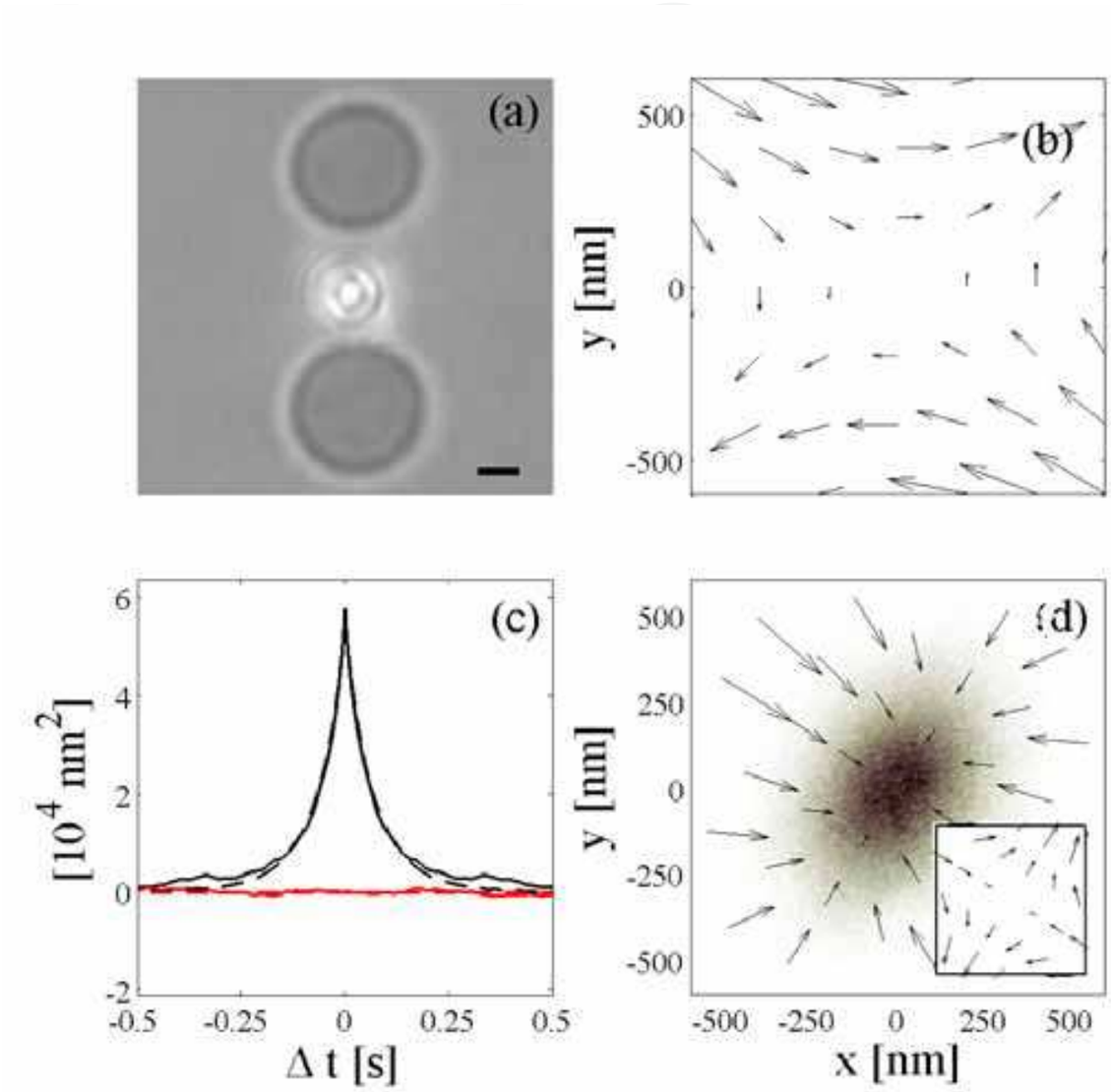

Fig. 7. Conservative force-field. (a) Experimental configuration with two spinning beads and (b) hydrodynamic component of the force-field (from hydrodynamic theory). (c) Experimental invariant functions $S_{ACF}(\Delta t)$ (black line) and $D_{CCF}(\Delta t)$ (red line) and their respective fitting to the theoretical shapes (dotted lines). (d) Experimental probability density function and reconstructed total force-field; inset: reconstructed hydrodynamic force-field.

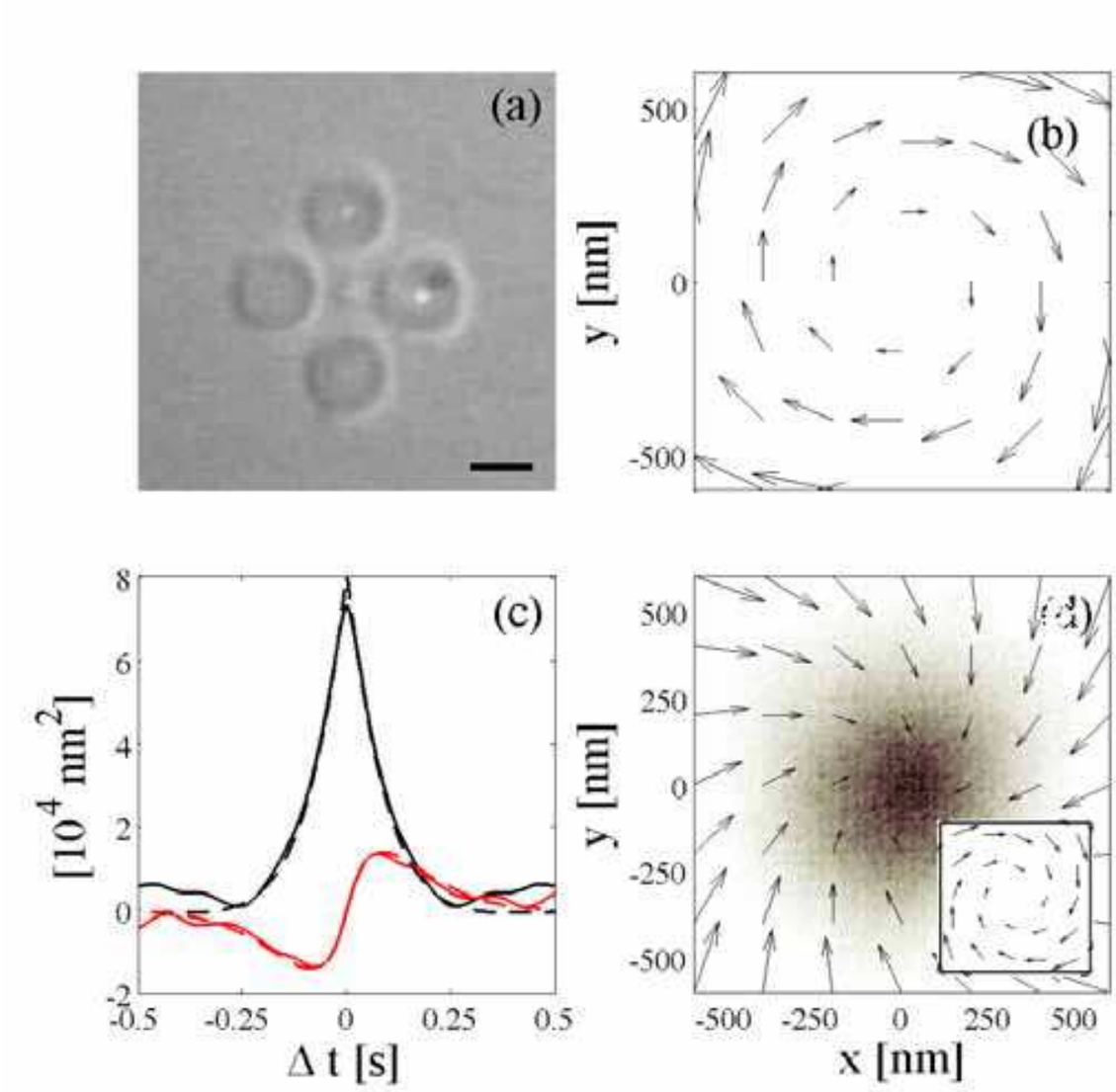

Fig. 8. Rotational force-field. (a) Experimental configuration with four spinning beads and (b) hydrodynamic component of the force-field (from hydrodynamic theory). (c) Experimental invariant functions $S_{ACF}(\Delta t)$ (black line) and $D_{CCF}(\Delta t)$ (red line) and their respective fitting to the theoretical shapes (dotted lines). (d) Experimental probability density function and reconstructed total force-field; inset: reconstructed hydrodynamic force-field.

6.1 Conservative force-field

In order to produce a conservative force-field, two CVCs are placed as shown in Fig. 7(a). In Fig. 7(b) the generated hydrodynamic force-field is presented as it is theoretically expected to be from hydrodynamic simulations. In Fig. 7(c), the invariant functions, $S_{ACF}(\Delta t)$ and $D_{CCF}(\Delta t)$ and their respective fitting to the theoretical shapes are presented. Since $D_{CCF}(\Delta t)$ is practically null, we see that in this case $\Omega = 0$, while the fitting to $S_{ACF}(\Delta t)$ allows one to

find the values of $\phi = 18s^{-1}$ and $\Delta\phi = 6s^{-1}$. The value of the rotation of the coordinate system in this case is $\theta = 32^{\circ}$.

The total force-field can now be reconstructed: $k_x = 225\,fN/\mu m$ and $k_y = 112\,fN/\mu m$. This force-field is presented in Fig. 7(d). The hydrodynamic force-field can now be retrieved by subtracting the optical force-field ($k_{opt} = 118\,fN/\mu m$ approximately constant in all directions), which can be measured in absence of rotation of the spinning particles (inset in Fig. 7(d)). This experimentally measured force-field corresponds very well to the theoretically predicted one (Fig. 7(b)).

6.2 Rotational force-field

In order to produce a rotational force-field, four CVCs are placed as shown in Fig. 11(a), which should theoretically produce the force-field presented in Fig. 8(b). In Fig. 8(c), the invariant functions, $S_{ACF}(\Delta t)$ and $D_{CCF}(\Delta t)$ and their respective fitting to the theoretical shapes are presented. Now $D_{CCF}(\Delta t)$ is not null any more and, therefore, it can be used to fit the three parameters: $\phi = 11s^{-1}$, $\Delta\phi \approx 0$ and $\Omega = 5rads^{-1}$. As already mentioned, $S_{ACF}(\Delta t)$ can be used for this purpose as well; however, using the latter, the sign of Ω stays undetermined.

The total force-field can now be reconstructed: $k_x \approx k_y = 100\,fN/\mu m$. This force-field is presented in Fig. 8(d). The hydrodynamic force-field can be obtained by subtracting the optical force-field ($k_{opt} = 78\,fN/\mu m$ approximately constant in all directions), which can be measured in absence of rotation of the spinning particles (inset in Fig. 8(d)). Again, this experimentally measured force-field corresponds very well to the theoretically predicted one (Fig. 8(b)).

7. Applications: measuring orbital angular momentum

A beam that carries an orbital angular momentum can induce a torque on the particle, which can be measured using the PTM. In the experiment fully presented in Ref. (Volpe & Petrov, 2006) the probe is trapped by a 785*nm* beam (Fig. 9(a)). We produced the Laguerre-Gaussian (LG) beam from a linearly polarized 532*nm* CW beam transformed by a holographic mask that generates a $l = 10$ order LG beam of power $P = 3mW$. The beam carries the flux of orbital angular momentum $\tau_{OAM} = lP/\omega = 7.5 \cdot 10^{-18} Nm$, where $\omega = 4 \cdot 10^{15} Hz$ is the light frequency. Only about 1% of the total flux of the orbital angular momentum is transferred to the dielectric sphere and only in the portion of the beam that overlaps the sphere. We estimate that in our experiments the beam transfers the torque $\tau_S = 7.5 \cdot 10^{-21} Nm$ to the sphere. A Dove prism can be inserted in the optical path to reverse the handedness of the helical phase front and therefore the sign of the orbital angular momentum without changing the direction or polarization of the beam.

In the absence of the 785*nm* optical trap (Fig. 9(b)) the 532*nm* beam moves the sphere towards the upper coverslip due to its radiation pressure and the gradient forces in the perpendicular plane do not allow the sphere to escape. In such conditions we can observe the clockwise and anti-clockwise rotation of the sphere depending on the handedness of the beam.

When the trapping 785*nm* beam power and therefore the trap stiffness are increased ($100\mu W$, $16fN/\mu m$), the sphere is more confined to the centre of the trapping beam (Fig.

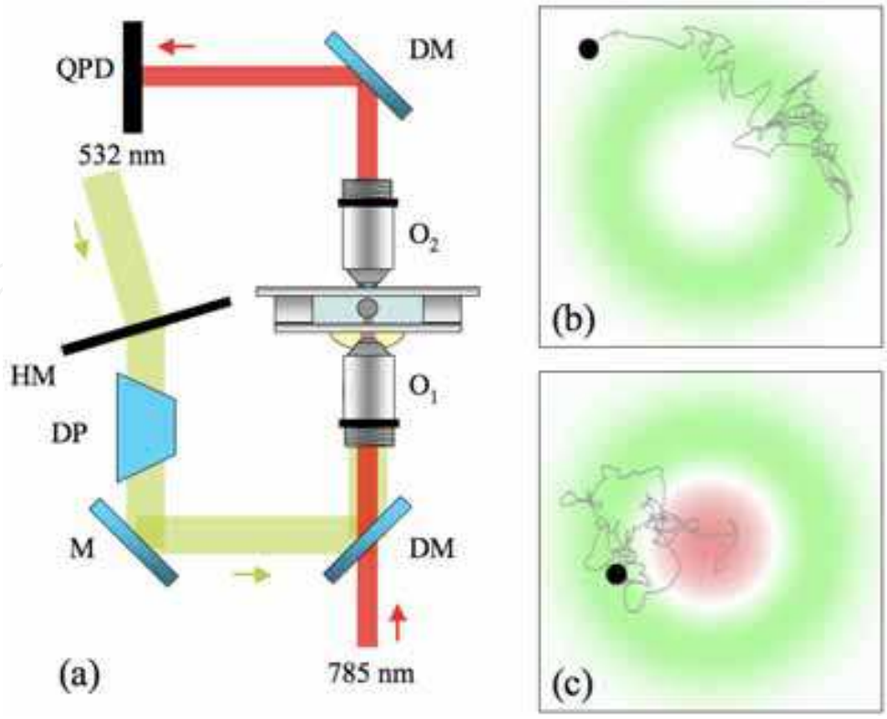

Fig. 9. Torque measurement setup. (a) Experimental setup: HM holographic mask, DP Dove prism, M mirror, DM dichroic mirror, O_1 focusing objective, O_2 collector objective, QPD quadrant photodetector. (b) Brownian motion of the sphere in the chamber when only the 532*nm* LG propagates. (c) Brownian motion of the sphere in the chamber when both the 532*nm* and the 785*nm* beams propagate.

9(c)) and does not display a rotational motion. We notice that in this case the Fourier analysis of the experimental traces does not show the presence of the torque existing in the system. However, the behaviour of the ACF and CCF functions near $\Delta t = 0$ (Fig. 10) unambiguously shows that the torque produced by the orbital angular momentum of the LG beam still affects the Brownian trajectories. Fitting these experimental functions to the theoretical ones and calculating the value of $\langle r^2 \rangle$ from the traces, we are able to measure the torque acting on the particle as $4.9 \pm 0.7 \cdot 10^{-21} Nm$.

8. Applications: non-conservative radiation forces in an optical trap

Back in 1992, Ashkin already pointed out that, in principle, scattering forces in optical tweezers do not conserve mechanical energy, and that this could have some measurable consequences (Ashkin, 1992). In particular, this nonconservative force would produce a dependence of the axial equilibrium position of a trapped microsphere as a function of its transverse position in the trapping beam (Fig. 11(a) and Fig. 10(c) of Ref. (Ashkin, 1992)); such prediction was first confirmed by Merenda and colleagues (Merenda et al., 2006). Recently, Roichman and colleagues (Roichman et al., 2008) have directly investigated the non-conservative component and discussed the implications that this might have for optical-tweezers–based experiments making use of the thermal fluctuations in the calibration procedure.

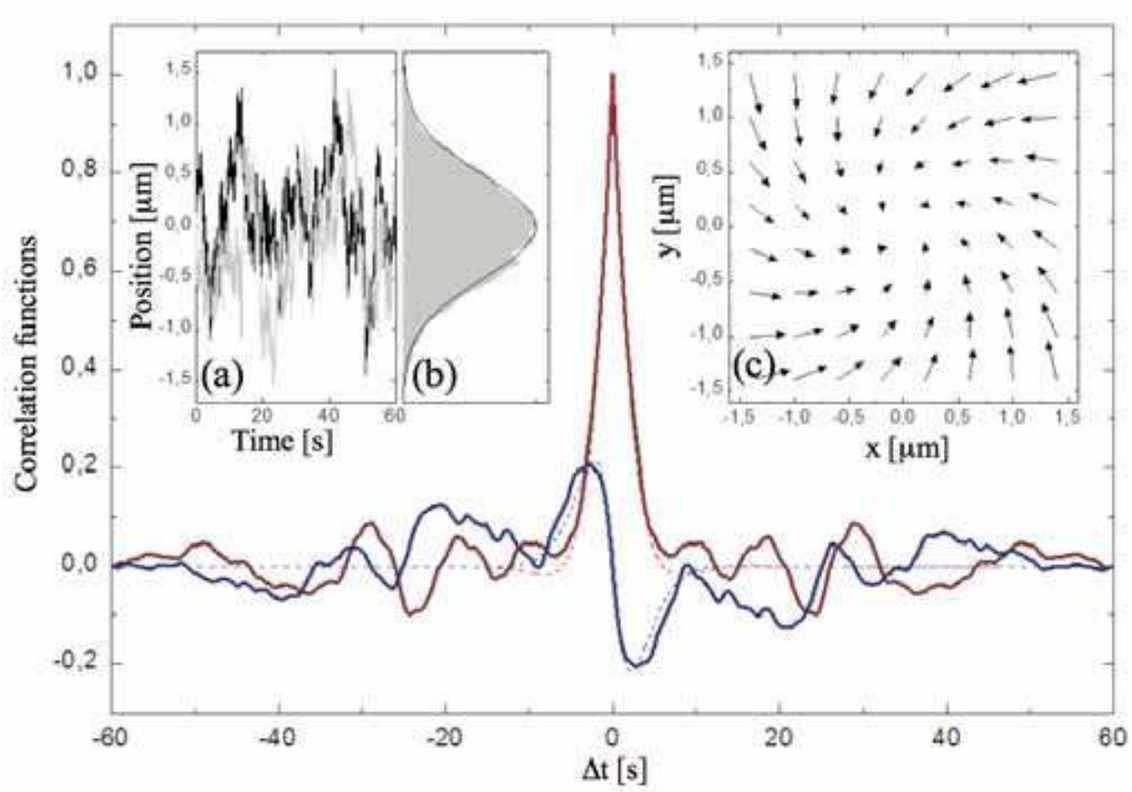

Fig. 10. Experimental ACF and CCF. Experimental ACF and CCF functions in presence of the torque induced by a LG beam with $l = +10$. The trap force constant k is high enough to confine the sphere. The continuous lines show the mean values obtained using five series of data acquisition (acquisition time $60s$, sampling rate $f_s = 1kHz$). The dotted lines show the fitting to the theoretical shape (the fitting was made on the central part of the curve for $\Delta t = [-2s, 2s]$). In the insets: (a), time traces for the x (black) and y (grey) coordinates; (b), histogram of the x coordinate and in black the fitting to a Gaussian distribution; and (c), vector force-field acting on the particle in the xy -plane.

Using the PTM we have evaluated the relative weight of the non-conservative component of the optical forces (Pesce et al., 2009). We used the PTM to analyze various optically trapped particles in different trapping conditions. The main result is that the non-conservative effects are effectively negligible and do not affect the standard calibration procedure, unless for extremely low-power trapping, far away from the trapping regimes usually used in experiments.

In Fig. 12, the ACFs and $D_{CCF}(\Delta t)$ are presented for a $0.45\mu m$ diameter particle held in an optical trap with an optical power at the sample of $6.0mW$. In order to have a non-vanishing $D_{CCF}(\Delta t)$, which is the signature of a rotational component of the force-field, the optical power at the sample needed to be reduced down to a few milliwatts. Notice that for this experiment the $D_{CCF}(\Delta t)$ is taken between the radial ($r = \sqrt{x^2 + y^2}$) and axial (z) coordinate. Furthermore, even under such low power a clearly non-vanishing $D_{CCF}(\Delta t)$ was

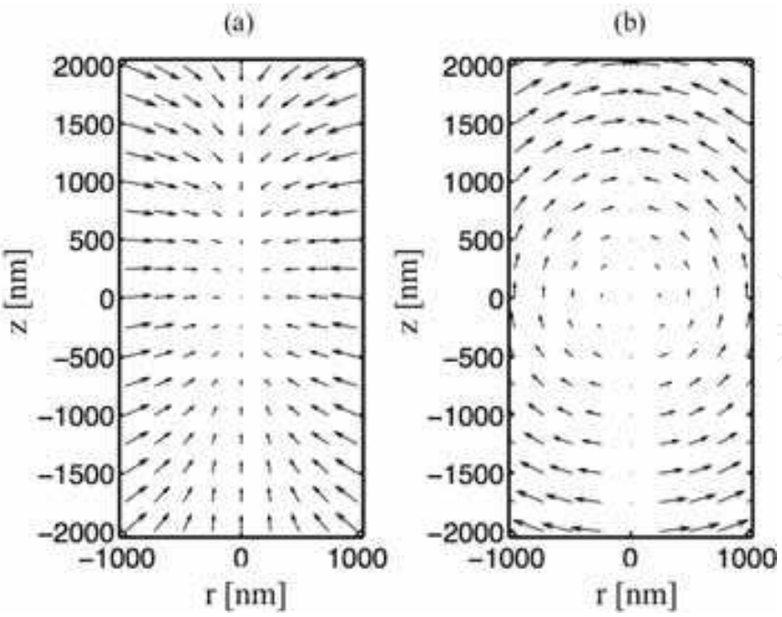

Fig. 11. Non-conservative radiation forces. (a) Force-field generated by an optical trap in the presence of a rotational component and (b) the rotational part of the force-field in the *rz*-plane. Note that for clarity of presentation the relative contribution of the non-conservative force-field has been exaggerated.

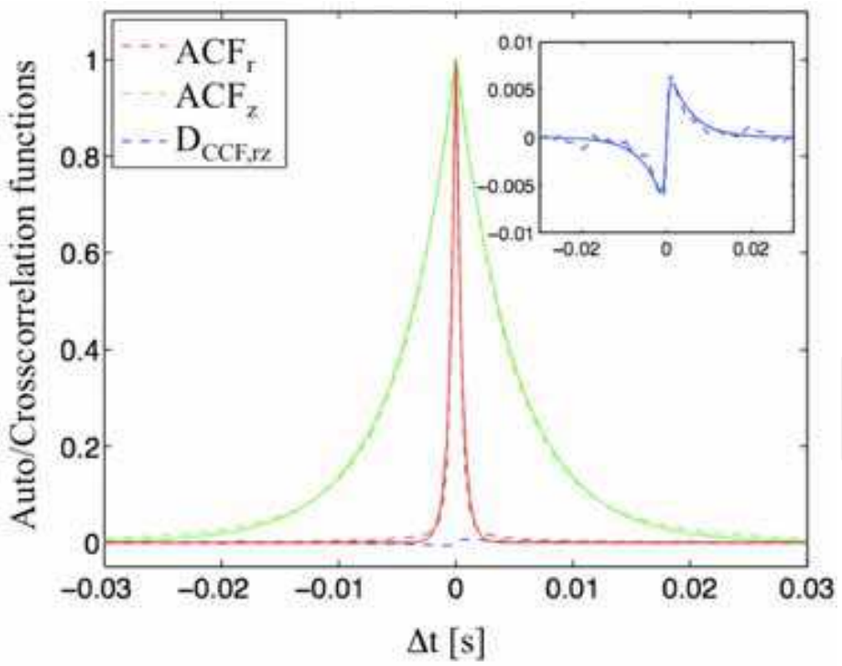

Fig. 12. Quantifying non-conservative radiation forces. ACF and $D_{CCF}(\Delta t)$ for a $0.45\,\mu m$ diameter colloidal particle optically trapped with a laser power of $6.0\,mW$ at the sample. Inset: Closeup of the $D_{CCF}(\Delta t)$. Dashed lines represent experimental data, while solid lines are the curves obtained from the fit.

only obtained when the acquisition time was increased up to $400s$. It is an important remark the fact that, due to the extremely low value of the rotational contribution to the total force-field, it is not immediately evident from the traces of the particle motion. Indeed the particle undergoes a random movement in the rz-plane, where it is not possible to distinguish the presence of a rotational component without the aid of a statistical analysis such as the one we propose.

9. Conclusion

The PTM technique can be applied to the detection of locally nonhomogeneous force-fields. This is achieved by analyzing the ACFs and CCFs of the probe position time series. We believe that this technique can help to gain new insights into microscale and molecular-scale phenomena. In these cases the presence of the Brownian motion is intrinsic and cannot be disregarded. Therefore this technique permits one to take advantage of the Brownian fluctuations of the probe in order to explore the force-field present in its surroundings. One of the most remarkable advantages of the technique we propose is that it can be implemented in all existing PFM setups and even on data acquired in the past. Indeed, it does not require changes to be made in the physical setup, but only to analyze the data in a new way. This method can even be applied to the study of the Brownian particle trajectories that can be obtained with techniques different from the PFM technique.

10. References

Ashkin, A. (1970). Acceleration and trapping of particles by radiation pressure. *Phys. Rev. Lett.*, 24, 156—159.

Ashkin, A (1992). Forces of a single-beam gradient laser trap on a dielectric sphere in the ray optics regime. *Biophys. J*, 61, 569—582.

Ashkin, A. (2000). History of optical trapping and manipulation of small- neutral particle, atoms, and molecules. *IEEE J Sel. Top. Quant. El.*, 6, 841—856.

Ashkin, A.; Dziedzic, J. M.; Bjorkholm, J. E. & Chu, S. (1986). Observation of a single-beam gradient force optical trap for dielectric particles, *Opt. Lett.*, 11, 288—290.

Babic, D.; Schmitt, C. & Bechinger, C. (2005). Colloids as model systems for problems in statistical physics. *Chaos*, 15, 026114.

Berg-Sørensen, K. & Flyvbjerg, H. (2004). Power spectrum analysis for optical tweezers, *Rev. Sci. Instrumen.*, 75, 594—612.

Berry, R. M. & Berg, H. C. (1997). Absence of a barrier to backwards rotation of the bacterial flagellar motor demonstrated with optical tweezers. *PNAS*, 94, 14433—14437.

Beth, R. A. (1936). Mechanical detection and measurement of the angular momentum of light. *Phys. Rev.*, 50, 115—125.

Bishop, A. I.; Nieminen, T. A.; Heckenberg, N. R. & Rubinsztein-Dunlop, H. (2004). Optical microrheology using rotating laser-trapped particles. *Phys. Rev. Lett.*, 92, 198104.

Block, S. M.; Goldstein, L. S. B. & Schnapp, B. J. (1990). Bead movement by single kinesin molecules studied with optical tweezers. *Nature*, 348, 348—352.

Bryant, Z.; Stone, M. D.; Gore, J.; Smith, S. B.; Cozzarelli, N. R. & Bustamante, C. (2003). Structural transitions and elasticity from torque measurements on DNA. *Nature*, 424, 338—341.

Bustamante, C.; Marko, J. F.; Siggia, E. D. & Smith, S. (1994). Entropic elasticity of lambda-phage DNA. *Science*, 265, 1599—1600.

Finer, J. T.; Simmons, R. M. & Spudich, J. A. (1994). Single myosin molecule mechanics: piconewton forces and nanometre steps. *Nature*, 368, 113—119.

Ghislain, L. P. & Webb, W. W. (1993). Scanning-force microscope based on an optical trap, *Opt. Lett.*, 18, 1678—1680.

Happel, J. & Brenner, H. (1983). Low Reynolds Number Hydrodynamics. Spinger, New York.

Huisstede, J. H. G.; van der Werf, K. O.; Bennink, M. L. & Subramaniam, V. (2005). Force detection in optical tweezers using backscattered light. *Opt. Express*, 13, 1113—1123.

La Porta, A. & Wang, M. D. (2004). Optical torque wrench: Angular trapping, rotation, and torque detection of quartz microparticles. *Phys. Rev. Lett.*, 92, 190801.

Lebedev, P. N. (1901). The experimental study of the pressure of the light. *Ann. Physik*, 6, 433—459.

Merenda, F.; Boer, G.; Rohner, J.; Delacrétaz, G. & Salathé, R.-P. (2006). Escape trajectories of single-beam optically trapped micro-particles in a transverse fluid flow. *Opt. Express*, 14, 1685—1699.

Metcalf, H. J. & van der Straten, P. (1999). Laser Cooling and Trapping. Springer, New York.

Neuman, K. C. & Block, S. M. (2004). Optical trapping, *Rev. Sci. Instrumen.*, 75, 2787—2809.

Nichols, E. F. & Hull, G. F. (1901). A preliminary communication on the pressure of heat and light radiation. *Phys. Rev.*, 13, 307—320.

Novotny, L.; Bian, R. X. & Xie, X. S. (1997). Theory of nanometric optical tweezers. *Phys. Rev. Lett.*, 79, 645—648.

Pesce, G.; Volpe, G.; De Luca, A. C.; Rusciano, G. & Volpe, G. (2009). Quantitative assessment of non-conservative radiation forces in an optical trap, *EPL*, 86, 38002.

Quidant, R.; Petrov, D. V. & Badenes, G. (2005). Radiation forces on a Rayleigh dielectric sphere in a patterned optical near field. *Opt. Lett.*, 30, 1009—1011.

Rohrbach A. & Stelzer, E. H. K. (2002). Three-dimensional position detection of optically trapped dielectric particles. *J Appl. Phys.*, 91, 5474—5488.

Roichman, Y.; Sun, B.; Stolarski, A. & Grier, D. G. (2008). Influence of Nonconservative Optical Forces on the Dynamics of Optically Trapped Colloidal Spheres: The Fountain of Probability, *Phys. Rev. Lett.*, 101, 128301.

Townes, C. H. (1999). How The Laser Happened. Oxford University Press, Oxford, UK.

Visscher, K.; Gross, S. P. & Block, S. M. (1996). Construction of multiple-beam optical traps with nanometer-resolution position sensing. *IEEE J Sel. Top. Quant. El.*, 2, 1066—1076.

Volke-Sepulveda, K.; Garcés-Chávez, V.; Chávez-Cerda, S. ; Arlt, J. & Dholakia, K. (2002). Orbital angular momentum of a high-order bessel light beam. *J Opt. B*, 4, S82—S89.

Volpe, G. & Petrov, D. (2006). Torque Detection using Brownian Fluctuations, *Phys. Rev. Lett.*, 97, 210603.

Volpe, G.; Quidant, R.; Badenes, G. & Petrov, D. (2006). Surface plasmon radiation forces. *Phys Rev. Lett.*, 96, 238101.

Volpe, G.; Volpe, G. & Petrov, D. (2007a). Brownian motion in a non-homogeneous force field and photonic force microscope, *Phys. Rev. E*, 76, 061118.

Volpe, G.; Kozyreff, G. & Petrov, D. (2007b). Back-scattering position detection for photonic force microscopy, *J Appl. Phys.*, 102, 084701.

Volpe, G.; Volpe, G. & Petrov, D. (2008). Singular point characterization in microscopic flows, *Phys. Rev. E*, 77, 037301.

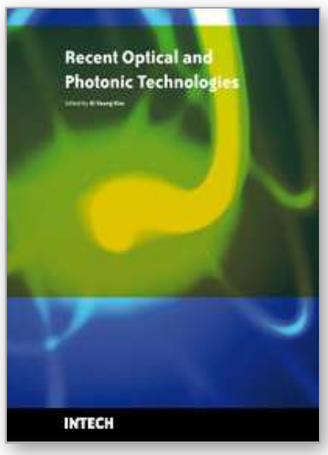

Recent Optical and Photonic Technologies

Edited by Ki Young Kim

ISBN 978-953-7619-71-8
Hard cover, 450 pages
Publisher InTech
Published online 01, January, 2010
Published in print edition January, 2010

Research and development in modern optical and photonic technologies have witnessed quite fast growing advancements in various fundamental and application areas due to availability of novel fabrication and measurement techniques, advanced numerical simulation tools and methods, as well as due to the increasing practical demands. The recent advancements have also been accompanied by the appearance of various interdisciplinary topics. The book attempts to put together state-of-the-art research and development in optical and photonic technologies. It consists of 21 chapters that focus on interesting four topics of photonic crystals (first 5 chapters), THz techniques and applications (next 7 chapters), nanoscale optical techniques and applications (next 5 chapters), and optical trapping and manipulation (last 4 chapters), in which a fundamental theory, numerical simulation techniques, measurement techniques and methods, and various application examples are considered. This book deals with recent and advanced research results and comprehensive reviews on optical and photonic technologies covering the aforementioned topics. I believe that the advanced techniques and research described here may also be applicable to other contemporary research areas in optical and photonic technologies. Thus, I hope the readers will be inspired to start or to improve further their own research and technologies and to expand potential applications. I would like to express my sincere gratitude to all the authors for their outstanding contributions to this book.

How to reference
In order to correctly reference this scholarly work, feel free to copy and paste the following:

Giovanni Volpe, Giorgio Volpe and Giuseppe Pesce (2010). The Photonic Torque Microscope: Measuring Non-Conservative Force-Fields, Recent Optical and Photonic Technologies, Ki Young Kim (Ed.), ISBN: 978-953-7619-71-8, InTech, Available from: http://www.intechopen.com/books/recent-optical-and-photonic-technologies/the-photonic-torque-microscope-measuring-non-conservative-force-fields

INTECH
open science | open minds

InTech Europe
University Campus STeP Ri
Slavka Krautzeka 83/A
51000 Rijeka, Croatia
Phone: +385 (51) 770 447
Fax: +385 (51) 686 166

InTech China
Unit 405, Office Block, Hotel Equatorial Shanghai
No.65, Yan An Road (West), Shanghai, 200040, China
中国上海市延安西路65号上海国际贵都大饭店办公楼405单元
Phone: +86-21-62489820
Fax: +86-21-62489821

IntechOpen

IntechOpen

© 2010 The Author(s). Licensee IntechOpen. This chapter is distributed under the terms of the Creative Commons Attribution-NonCommercial-ShareAlike-3.0 License, which permits use, distribution and reproduction for non-commercial purposes, provided the original is properly cited and derivative works building on this content are distributed under the same license.

IntechOpen

IntechOpen